

Design of Oxygen Vacancy Configuration for Memristive Systems

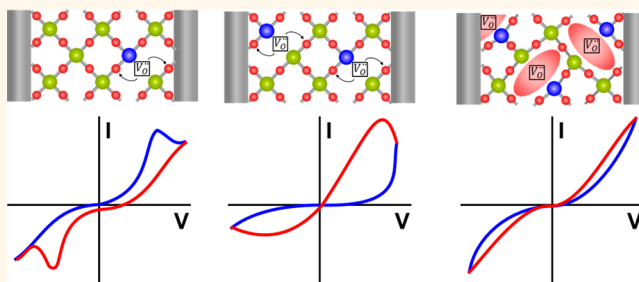
Rafael Schmitt,[†] Jonathan Spring,[†] Roman Korobko,[†] and Jennifer L.M. Rupp^{*,†,‡,§,¶}

[†]Electrochemical Materials, Department of Materials, Swiss Federal Institute of Technology, ETH Zurich, Hönggerbergstr. 64, Zurich 8093, Switzerland

[‡]Laboratory of Electrochemical Materials, Department of Materials Science and Engineering, Massachusetts Institute of Technology, Cambridge, Massachusetts 02139, United States

S Supporting Information

ABSTRACT: Oxide-based valence-change memristors are promising nonvolatile memories for future electronics that operate on valence-change reactions to modulate their electrical resistance. The memristance is associated with the movement of oxygen ionic carriers through oxygen vacancies at high electric field strength *via* structural defect modifications that are still poorly understood. This study employs a $\text{Ce}_{1-x}\text{Gd}_x\text{O}_{2-y}$ solid solution model to probe the role of oxygen vacancies either set as “free” or as “immobile and clustered” for the resistive switching performance. The experiments, together with the defect chemical model, show that when the vacancies are set as “free”, a maximum in memristance is found for 20 mol % of $\text{GdO}_{1.5}$ doping, which clearly coincides with the maximum in ionic conductivity. In contrast, for higher gadolinia concentration, the oxide exhibits only minor memristance, which originates from the decrease in structural symmetry, leading to the formation of “immobile” oxygen defect clusters, thereby reducing the density of mobile ionic carriers available for resistive switching. The research demonstrates guidelines for engineering of the oxide’s solid solution series to set the configuration of its oxygen vacancy defects and their mobility to tune the resistive switching for nonvolatile memory and logic applications.



KEYWORDS: resistive switching, memristor, ceria, oxygen vacancies, Raman

The miniaturization of silicon-based electronics has been the key to increased digital performance, enabling the density of transistors per chip to double every 18 months.¹ However, transistor scaling reaches physical limits, and it becomes more and more difficult to process information based on the storage of electronic charges at dielectric interfaces.² Those challenges will have to be overcome by material and technology innovations, searching for carriers other than electrons to store and process information, such as ions in novel types of ionically driven memory storage.

Resistive switches operating on ionic carriers, also named memristive devices, have the potential to replace today’s technology, enabling novel memory and computing architectures circumventing the von Neumann bottleneck.³ They are simple structures in which the switching material is sandwiched between two electrodes. Oxide-based valence-change memories (VCMs) are one type of memristive device, where variations in the resistivity can be induced by redox reactions in the oxide or at the oxide–electrode interfaces for a given voltage pulse. Herein, an applied high electric field in the range of MV/m enables the motion of oxygen ions in the device. As a result, a nonvolatile, polarity-dependent modulation of the electrical resistance can be measured through a hysteretic current–

voltage profile.^{4–6} In the past years, extensive demonstrations on resistive switching in oxides were realized, mostly on TiO_2 ,⁷ HfO_2 ,⁸ Ta_2O_5 ,⁹ and SiO_2 ¹⁰ being classic gate oxides in today’s semiconductor industry besides some perovskites.¹¹ Many of these experiments demonstrate the hysteretic current–voltage relationship or pulsed switching, which is of fascination for electrical engineers, but only few describe the defect chemistry or kinetics that drive the resistive switching processes. It is also worth noticing that virtually no extrinsic doping studies exist for which, from a defect chemical point of view, the balance of ionic and electronic carriers as mobile defects is systematically tailored for the oxide to study their implication on resistive switching.

Modulation of Intrinsic and Extrinsic Defects for Resistive Switching Oxides. Numerous reports show that oxygen vacancies play a role as defects for the resistive switching mechanism;^{12–14} they can be present as extrinsic or intrinsic defects depending on whether they are induced by

Received: May 5, 2017

Accepted: August 29, 2017

Published: August 29, 2017

dopants or not. Despite the qualitative acknowledgment, it remains unclear in which manner the concentration and mobility of oxygen vacancies of the oxide affect the resistive switching property for the memristive devices under bias.

Intrinsic oxygen vacancy defects can be varied by modifying the thin film deposition conditions (e.g., temperature, oxygen partial pressure)^{15,16} or by postannealing of an oxide film.^{17,18} For example, Bae *et al.* observed an improvement of the resistive switching uniformity at a critical oxygen content adjusted during deposition of TiO_{2-x} films.¹⁵ Similar results were shown by Kwak *et al.* on Ar-annealed CoO_x devices in which a change in the Co valence was observed by X-ray photoelectron spectroscopy.¹⁸ Lower forming voltage but similar resistive switching performance was achieved by Sharath *et al.* by modulating the oxygen-deficient growth of HfO_{2-x} devices for which hard X-ray photoelectron spectroscopy revealed the presence of defect states in the valence band.¹⁶ Younis *et al.* interpreted the loss in resistive switching of electrodeposited CeO₂ films to a depletion of oxygen vacancies after annealing at 300 °C, as confirmed by X-ray photoelectron spectroscopy.¹⁷

It can be concluded from those studies on intrinsic oxygen defect modulations that the resistance ratio, as well as the forming and switching variability, is affected by the amount of oxygen vacancy defects available in the device's oxide constituent. On the other hand, the intrinsic oxygen non-stoichiometry of undoped switching oxides is very difficult to control. It relies heavily on the external processing parameters at the oxide's film growth. Also, the impurity level might play a significant role on the defect states. These limitations can be circumvented by using extrinsic dopants to control the level of oxygen stoichiometry and defects for memristors.

Extrinsic oxygen vacancy defects in anionic memristive devices were reported to alter the resistive switching behavior of NiO,¹⁹ HfO₂,²⁰ or Ta₂O₅.²¹ Li *et al.* demonstrate that Cu doping of up to 2 atom % enhances the electronic carrier mobility in NiO by a factor of 3 and can be used to decrease the set voltage of the resistive switch.¹⁹ The oxygen vacancy formation energy in HfO₂ could be lowered through the extrinsic doping with trivalent cations on the four-valent Hf lattice sites, enabling a better control of the conductive filament formation.²⁰ Furthermore, the oxygen transport in Ta₂O₅ is enhanced through the doping with Si, by creating oxygen vacancy transport channels leading to a more controllable resistive switching.²¹

Summarizing literature, these studies deal primarily with low doping concentrations. With higher doping and oxygen vacancy concentrations, the effect of defect interactions such as oxygen vacancy dopant clustering on resistive switching needs to be considered, which has, however, only sparsely been reported. For example, two resistive switching time scales were observed for epitaxial La_{0.5}Ca_{0.5}MnO₃ thin films and explained based on the motion of free and clustered oxygen vacancies having different migration energy barriers.²² However, a clear defect model describing formation and dissolution of vacancy clusters within a solid solution series is missing.²² Similarly, the importance of including free oxygen vacancies *versus* defect clusters for the resistive switching model of nonstoichiometric SrTiO₃ was proposed by Kim *et al.* without going into the details of the resistive switching mechanism.²³ Yet, no study has been performed where memristive devices with and without clustered oxygen vacancies were tailored in a systematic manner by solid solution variations of the resistive switching oxide.

Analyzing the reports on extrinsic doping in the field of resistive switching, we draw three main observations.

(i) Although efforts exist to add an extrinsic dopant to a host lattice, systematic studies in which the extrinsic dopant is varied over a wide solubility limit are missing. This is surprising as the direct implication from a defect chemical point of view is to tune effectively the oxygen vacancy concentration and mobility in the host lattice, which defines the characteristics of a memristive device, such as the switching speed, the $R_{\text{OFF}}/R_{\text{ON}}$ resistance ratio, or the number of addressable states.

(ii) Resistive switches operating on oxygen vacancies have not been studied with respect to systematic variations of their free and associated defect levels for oxygen vacancies. Knowledge on how free *versus* frozen oxygen vacancies are connected to the resistive switching performance may be key to optimize those oxides for future memory and computing architectures.

(iii) Extrinsic doping may be an excellent way to increase the reservoir of available oxygen vacancies as defect sites for ions to hop and to engineer the resistive switching response. Nevertheless, it remains unclear if local lattice distortions and symmetry breaks, induced by oxygen vacancy concentration changes, modify the current–voltage profile in its resistive switching performance.

Gadolinia-Doped Ceria Solid Solution Series To Tailor the Mobility and Configuration of Oxygen Defects for Resistive Switching Devices. Among the plethora of metal oxide materials, gadolinia-doped ceria exhibits one of the highest ionic conductivity values and forms a stable solid solution series over a wide compositional range. The defect chemistry of that mixed oxygen ionic-electronic conductor has been widely studied.²⁴ Additionally, it is known that the conductivity in reduced gadolinia-doped ceria is mainly of electronic nature at room temperature and takes place over small polaron transport,²⁵ which makes it a particularly interesting model system for our work to tune the oxygen defects in view of their impact on the resistive switching properties.

Ceria has a high reduction potential and remains in the *fluorite* phase (*Fm3m* space group) over a broad temperature and oxygen partial pressure range.²⁴ It is an established material in numerous applications such as catalysts,^{26–28} solid oxide fuel cell electrolytes,^{29,30} sensors,^{31,32} and solar-to-fuel applications.^{33,34} Extrinsic doping of ceria with aliovalent cations goes along with the creation of charge-compensating oxygen vacancies. The detailed defect chemistry for the solid solution of gadolinia-doped ceria is presented in [Supporting Information S1](#). The ionic conductivity can be easily altered through extrinsic doping of ceria with lower valent elements, such as Gd³⁺,^{24,35} without undergoing a change in either the crystal structure or the band gap.³⁶

At low doping concentrations <20 mol %, Gd³⁺ cations randomly substitute the Ce⁴⁺ host in the *fluorite* lattice structure, forming a solid solution and, therefore, increasing the concentration of free oxygen vacancies. This leads to an increase in the ionic conductivity.

At intermediate doping concentrations >20 mol %, interaction between the defects is expected, thus forming associates such as charged dimers $[\text{Gd}'_{\text{Ce}}\text{V}^{\bullet\bullet}]^{\bullet}$ and neutral trimers $[2\text{Gd}'_{\text{Ce}}\text{V}^{\bullet\bullet}]^{\times}$. Larger associates show an increased stability, and hence it is energetically more favorable for the oxygen vacancies to order, forming clusters with *bixbyite* structure as probed by means of TEM³⁷ and confirmed by computational results.³⁸ For gadolinia

Table 1. Exemplary Overview of Ceria-Based Single Films and Multilayer Structures Employed as Oxides in Memristive Devices, Their Resistive Switching Characteristics, and Microstructures

Switching Oxide Material	$R_{\text{OFF}}/R_{\text{ON}}$ Ratio	Switching Voltage	Electroforming		Oxide Microstructure	Device Geometry	Film Deposition Technique	Ref.
			Yes	No				
CeO ₂	10	2.8	X		-	Cross-plane	E-beam	58
		10	X		Epitaxial			59
	4	3		X	-		Electrodeposition	17
	100	1.5	X		Polycrystalline		Pulsed laser deposition	60
	500	2			Epitaxial			61
	1000	4	X		Polycrystalline			62
	100'000	3			Epitaxial			63
	50'000	1.8			Epitaxial			64
		1.5			-			47
	40	0.6	X		Polycrystalline		RF-sputtering	65
	100	2	X		-			66
	10'000	2		X	Amorphous			67
	100'000	1	X		Polycrystalline			45
Ce _{1-x} Co _x O ₂	1'000	2.2			Nanorods	Cross-plane	Electrochemical deposition	68
CeO ₂ / La _{0.8} Sr _{0.2} MnO ₃	10'000	2	X		-	In-plane	Atomic layer deposition	48
Ce _{0.9} Gd _{0.1} O _{1.95} / Er ₂ O ₃	15	200	X		Oriented	Cross-plane	Pulsed laser deposition	44
CeO ₂ / La _{0.7} (Sr _{0.1} Ca _{0.9}) _{0.3} MnO ₃	100	4			-			69
CeO ₂ / ZnO	4'000	5			Polycrystalline		70	

doping, the appearance of the *bixbyite* structure at 20 mol % of GdO_{1.5} coincides with the highest ionic conductivity measured experimentally.^{35,39,40}

For high doping concentrations >25 mol %, a full secondary phase transformation from the original *fluorite* to a *bixbyite* structure is observed.⁴¹ In this state, the lowered symmetry implies nonequivalent lattice positions for the ions, where the oxygen vacancies become immobile occupying particular Ce-neighborly sites. This reduces the concentration of free oxygen vacancies in the lattice and thus increases the activation energy lowering the ionic conductivity.^{39,41,42}

The transition from *fluorite* to *bixbyite* structure is not easily observable by X-ray diffraction (XRD) due to the low scattering power of oxygen and the not necessarily long-range periodic oxygen vacancy ordering. Raman spectroscopy on the other hand probes the near-order bond vibrations, which makes it a powerful technique to probe the local structural transition and symmetry breaks for gadolinia-doped ceria.^{43,44} Thus, gadolinia-doped ceria is an ideal model system giving the opportunity to study the role of oxygen vacancies on (i) ionic transport and (ii) local near-order distortions ranging from *fluorite* to *bixbyite* structures. This motivates us to look into the potential of ceria-based resistive switching devices by giving an overview of the field.

Undoped ceria films as well as multilayers of ceria and additional transition metal oxides have been successfully used for resistive switching devices and show memristive behavior. Single ceria layers as resistive switches were demonstrated in sputtered, polycrystalline ceria films with a $R_{\text{OFF}}/R_{\text{ON}}$ resistance ratio reaching 10⁵ and a retention time exceeding 10⁴ s.⁴⁵ These are very promising results when comparing to state-of-the-art SrTiO₃ exhibiting a resistance ratio of 10³ and retention times of 10⁵ s.⁴⁶ However, no information on the structural modifications associated with the resistance change is given. In contrast, Gao *et al.* demonstrated using *in situ* transmission electron microscopy that the resistive switching effect in CeO₂ is based on migration of oxygen vacancies and the reversible valence change between Ce⁴⁺ and Ce³⁺ associated therewith, which increases the electronic conductivity.⁴⁷ Importantly, electron diffraction studies revealed that in the low resistive state, oxygen vacancies reorder, transferring the crystal structure

from a *fluorite*- to a *bixbyite*-type; *viz.* highly reduced Ce₂O₃ prevails for that latter state.

Multilayer resistive switches using ceria as an interfacial layer in combination with La_{0.8}Sr_{0.2}MnO₃, commonly used as an electrode, were shown to lower the operation voltage from 10 to 3 V by acting as an oxygen reservoir.⁴⁸ Very recently, Schweiger *et al.* demonstrated memristive devices based on interfacial strain engineered Ce_{0.9}Gd_{0.1}O_{1.95-δ}/Er₂O₃ multilayers.⁴⁴ A pronounced reduction, symmetry lowering and thereby increased oxygen vacancy concentration was engineered close to the largely strained gadolinia-doped ceria interfaces in the multilayer and studied by two independent methods, being TEM and Raman spectroscopy. Importantly, it was demonstrated that the magnitude of strain opposed at the Ce_{0.9}Gd_{0.1}O_{1.95-δ} phase alters the memristive response of the device and can be used as a tool.⁴⁴

We summarize and give an overview of ceria-based memristive devices and their characteristics in Table 1. To date, mostly undoped ceria was used with epitaxial, polycrystalline, and amorphous microstructures for single films. Irrespectively of the thin film deposition technique, an electroforming step is required in most cases to induce resistive switching, giving rise to a wide range of resistance ratios from 4 to 10⁵ at switching voltages between 0.6 and 200 V (respectively, 5–600 MV/m). Electrical characterization is mostly limited to current–voltage measurements, completed by additional pulsing in selected cases. When comparing the multilayer devices, it is evident that both the switching voltages as well as the resistance ratios are comparable to values obtained in the single-layer devices. It can be concluded that resistive switching is found in devices using ceria as single- or multilayer switching oxide material with promising resistance ratios down to switching voltages of 0.6 V. However, it remains open how the resistive switching is affected by ionic mobility and defect association for extrinsically doped ceria-based resistive switches.

In this work, we design resistive switching devices employing a solid solution series for the oxide to capture the implication of having the oxygen vacancies defined as “free” or “frozen” defects on the resistive switching properties. For this, we tailor as a model material the gadolinia concentration as an extrinsic

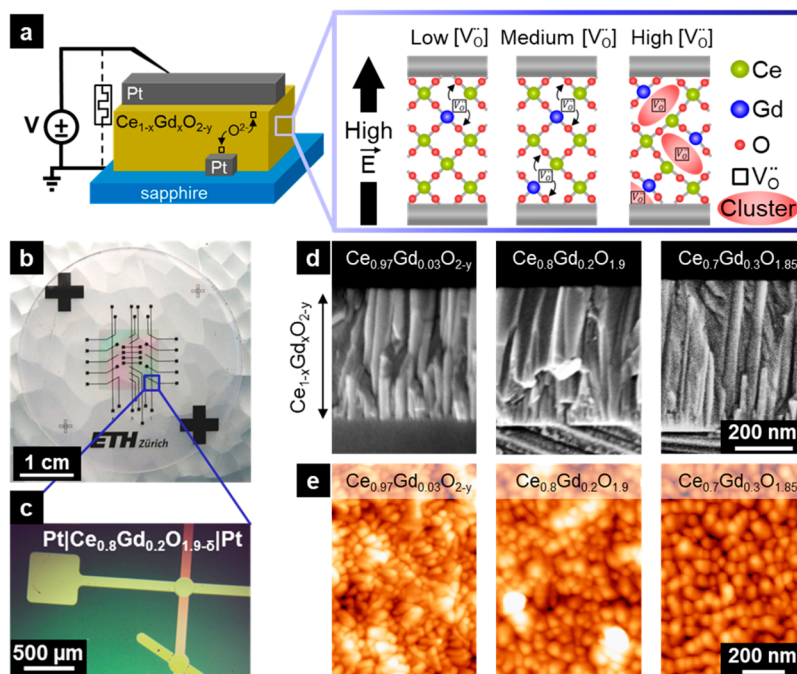


Figure 1. Gadolinia-doped ceria devices as a model system to study the role of oxygen vacancy concentration and configuration in resistive switching. (a) Schematic representation of a single Pt|Ce_{1-x}Gd_xO_{2-y}|Pt device cross section and the defect states. (b) Photograph of a sample showing the different crossbar switching units. (c) Optical micrograph of individual switching units. (d) Scanning electron microscopy picture of a thin film cross-view. (e) Surface topography measured by atomic force microscopy.

dopant in the resistive switching oxide ceria. Through this strategy, we can track the oxygen transfer dynamics on the resistive switching response and probe *via* Raman spectroscopy the level of lattice distortions and symmetry breaks upon a systematic tailoring of the oxygen vacancy level and association degree. We unequivocally demonstrate by the defect chemical model oxide structures that it is not only the presence of oxygen vacancies but their concentration and degree of structural association that defines the resistive switching property in view of high-performance memristive devices.

RESULTS AND DISCUSSION

Gadolinia-Doped Ceria as Defect Chemical Model Oxides for Memristive Devices. We fabricate memristive device units composed of gadolinia-doped ceria oxides with crossbar Pt electrode structures to study the influence of extrinsic doping, oxygen vacancy formation, and association on the resistive switching property (Figure 1a). In Figure 1b,c, we display the successful fabrication of an array of Ce_{0.8}Gd_{0.2}O_{1.9-δ} switching units with crossbar Pt electrodes integrated on a sapphire substrate. The two-terminal devices consist of microfabricated circular-shaped Pt electrodes oriented in cross-plane geometry *versus* the oxide thin film (Figure 1c). Solid solution tailoring of the oxide thin film defines the concentration of the *extrinsic dopant* gadolinia in the ceria lattice, which we vary between 3 and 30 mol % of GdO_{1.5}. The extrinsic defect level concentration serves to impose three possible defect chemical scenarios on the oxygen vacancies of the oxides in the memristive units: (i) At low extrinsic doping level (<10 mol %), a generally minor concentration of extrinsic oxygen vacancy defects is formed; *viz.* the reservoir of present oxygen vacancy defects to contribute in resistive switching is set as low. (ii) At intermediate extrinsic doping level (10–20 mol %), we form a high concentration of soluble oxygen

vacancies by dopant host substitution and have an optimum oxygen ionic mobility in the lattice. (iii) At high extrinsic doping level (>20 mol %), the dopant cation is easily clustered with an oxygen vacancy due to lattice instabilities and forms associated defects for lowered oxygen ionic mobility.

Analyzing the microstructure of the device cross sections by scanning electron microscopy (SEM) (Figure 1d), which exemplarily shows the results for *low*, *intermediate*, and *high* gadolinia doping concentrations, we conclude that the active oxide thin films grow in a dense, columnar, and crack-free microstructure over all investigated doping concentrations. All deposited films exhibit a total thickness of about 500 nm ($\pm 10\%$). The surface topography was measured by atomic force microscopy (AFM) (Figure 1e). We observe a similar surface roughness of 3.8 nm independent of the extrinsic doping concentration. An average grain size of 50 nm is measured both by AFM and SEM for all compositions. XRD confirms a cubic crystal structure with *Fm* $\bar{3}$ *m* symmetry with strong orientation along the (111) crystallographic axis (see Supporting Information S2).

Vibrational Raman Spectroscopy of Solid Solution Tailored Ce_{1-x}Gd_xO_{2-y} Thin Films. Raman spectroscopy has been employed to study the vibrational modes of oxygen–cation bonds as a function of extrinsic doping. The energy of the vibrational Raman modes is measured by the relative wavenumber shift to the incoming wavelength (see schematic Figure 2a). Here, we apply Raman spectroscopy to the memristive devices to probe the ionic near-order correlations relative to the extrinsic doping over a wide range from 3 to 30 mol % of GdO_{1.5} in ceria (Figure 2b). Importantly, the technique allows one to probe the cation–anion interaction and is also sensitive to changes in the oxygen sublattice itself. Because the oxygen ionic transport is largely driven by the

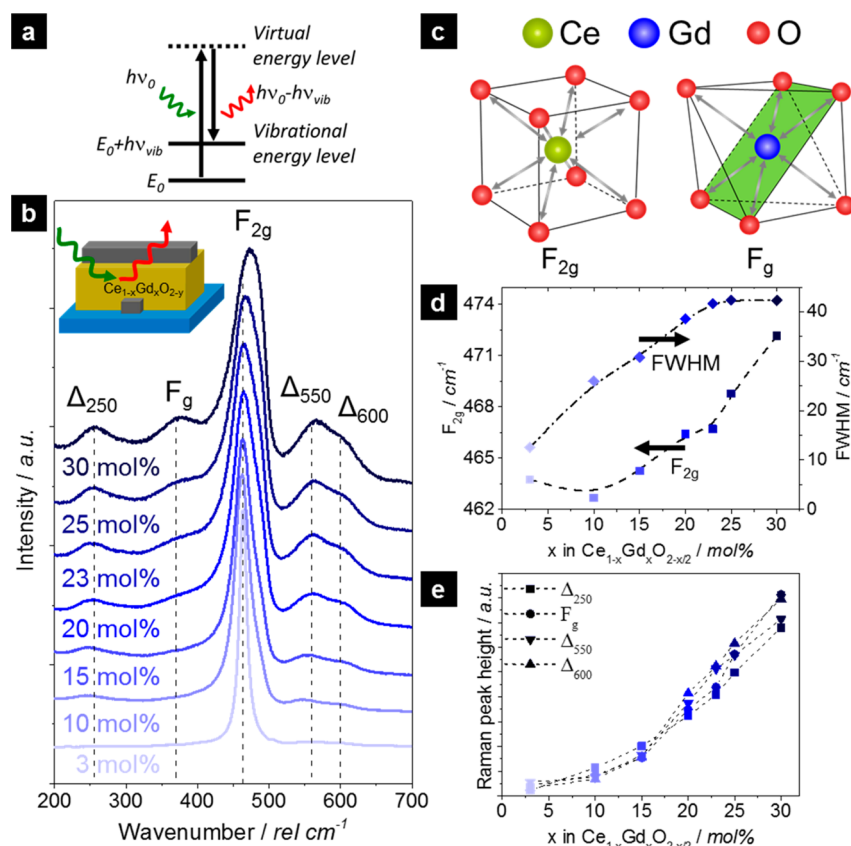


Figure 2. Near-order structural analysis of the gadolinia-doped ceria model switching devices using Raman spectroscopy. (a) Schematic representation of the Raman spectroscopy principle. (b) Raman spectra of the $\text{Ce}_{1-x}\text{Gd}_x\text{O}_{2-y}$ devices with $\text{GdO}_{1.5}$ doping concentrations of 3–30 mol %, showing near-order changes in the bonding environment. F_{2g} and F_g denote the vibrational symmetry, whereas Δ_{250} , Δ_{550} , and Δ_{600} denote the defect-activated bands. (c) Bonding environment of the F_{2g} and F_g Raman mode in the *fluorite* ceria and *bixbyite* gadolinia, respectively. (d) Peak position (left y-axis) and fwhm (right y-axis) of the 465 cm^{-1} Raman vibration with F_{2g} symmetry for the gadolinia-doped ceria solution series; the lines serve as a guide for the eyes. (e) Peak intensity of the oxygen vacancy induced Raman vibrations denoted as Δ_{250} , Δ_{550} , and Δ_{600} ; the lines serve as a guide for the eyes.

oxygen vacancy surrounding, this allows relevant structural information to be obtained.

We analyze first the low 3 mol % of $\text{GdO}_{1.5}$ -doped ceria thin film of the resistive switching devices (Figure 2b). The spectrum is characterized by a peak around 464 cm^{-1} corresponding to the oxygen breathing mode around the Ce^{4+} cation with F_{2g} symmetry (see ref 49 for details). Due to the high symmetry, this triply degenerate mode is the only Raman-active vibration for the *fluorite* crystal structure. The bonding environment of the eight-fold coordinated Ce^{4+} is exemplified in Figure 2c, and the corresponding Raman-active vibrational bonds are indicated by arrows. The selected dopant Gd_2O_3 , on the other hand, crystallizes in the cubic *bixbyite* structure ($Ia\bar{3}$ space group),⁵⁰ in which the cation is octahedrally coordinated, giving rise to 22 Raman-active modes: $4A_g + 4E_g + 14F_g$,⁵¹ from which the most intense band around 360 cm^{-1} is of F_g symmetry.⁵²

Increasing the extrinsic doping concentration of the oxide for the switching device structures results in a frequency shift for which we distinguish two basic regimes:

(i) Raising the gadolinia doping concentration up to 10 mol % leads to a vibrational frequency decrease of the F_{2g} active Raman band to 462.7 cm^{-1} (Figure 2d). (ii) In contrast, further doping up to 30 mol % of $\text{GdO}_{1.5}$ in ceria results in a significant linear increase of the F_{2g} Raman wavenumber toward 472.2 cm^{-1} for the oxide film structures. The steady increase of the

fwhm of the F_{2g} mode reflects the higher degree of structural disorder induced by the gadolinia dopant and reaches a plateau for $\text{GdO}_{1.5}$ doping concentrations exceeding 20 mol %. As the fwhm levels off, the high-frequency shift of the F_{2g} band becomes more significant.

Analyzing the spectra in more detail for dopings above 3 mol %, we see the rise of additional bands Δ_{250} , Δ_{550} , and Δ_{600} at 250, 550, and 600 cm^{-1} , respectively. Careful analysis reveals that these originate from the presence of oxygen vacancies and the associated symmetry reduction in agreement with earlier findings on doped ceria pellets.^{42,53} These vibrational modes are activated through the lowered local symmetry induced by the presence of oxygen vacancies and the different size of the Gd^{3+} versus Ce^{4+} cations and show increasing Raman activity as the extrinsic doping with $\text{GdO}_{1.5}$ exceeds 10 mol % (Figure 2e). We interpret this as the homogeneous incorporation of gadolinia into the CeO_2 crystal structure of the films and the formation of oxygen vacancies associated therewith. For $\text{GdO}_{1.5}$ concentrations larger than 20 mol %, an additional band occurs at about 370 cm^{-1} , which coincides with the F_g mode of Gd_2O_3 ⁵² reflecting the onset of the *bixbyite*-like oxygen vacancy ordering.^{42,54}

The results show that upon a critical extrinsic $\text{GdO}_{1.5}$ doping of 20 mol %, the *fluorite* structure type prevails, and as a consequence, predominantly “free” oxygen vacancies form, characterized by a low uprise of the Δ_{250} , Δ_{550} , and Δ_{600} bands

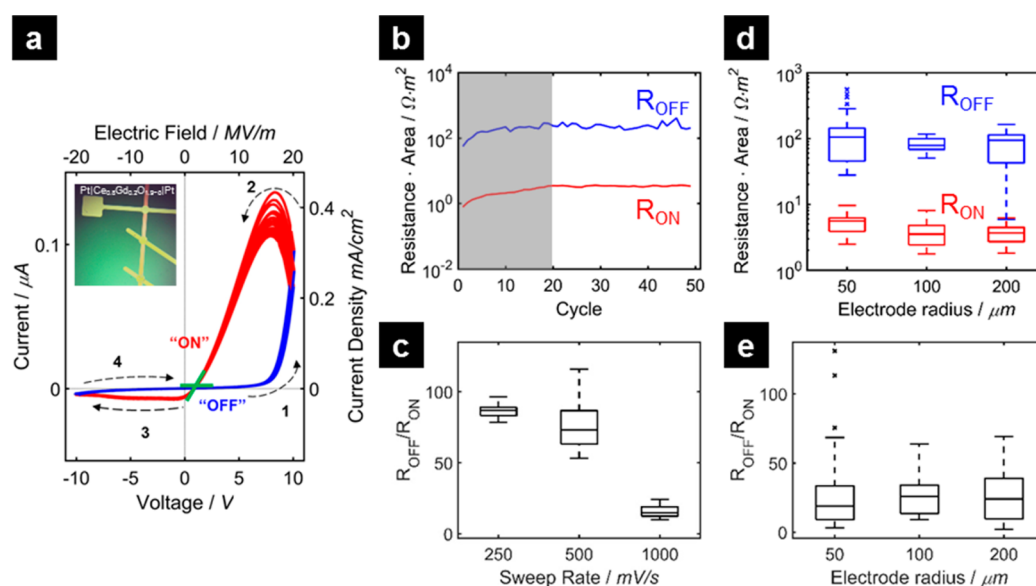


Figure 3. Resistive switching characteristics of a Pt–Ce_{0.8}Gd_{0.2}O_{1.9- δ} –Pt crossbar device. (a) Hysteretic current–voltage curve is showing the switching from the high-resistive “OFF”-state to the low-resistive “ON”-state for positive bias with a $R_{\text{OFF}}/R_{\text{ON}}$ resistance ratio of 60. (b) Resistance \times area values of the device measured in (a) shown over 50 cycles. After 20 cycles, the values level off toward a stable value. (c) Sweep rate dependence of the resistance ratio. (d) Electrode area dependence of the resistance \times area for both the high-resistive “OFF”-state and the low-resistive “ON”-state. (e) $R_{\text{OFF}}/R_{\text{ON}}$ resistance ratio for various electrode sizes of the values shown in (d).

in Raman. This changes with the appearance of the *bixbyite* structure for more than 20 mol % of GdO_{1.5}. Here, the lattice instability leads to defect clusters measurable in the rise of the F_g band intensity correlating to the *bixbyite* structure. Now it is important to note that the trend reported here on the defect chemistry of the switching oxide films by Raman spectroscopy relates very well to electrochemical studies for which a maximum in ionic conductivity clearly exists in doped ceria at 20 mol % for the *fluorite* structure type.³⁹ At this point, the magnitude in “free” vacancies is largest, and the oxygen ions can hop best and in quantity over these like a freeway. As soon as clusters with *bixbyite* structure form in the oxide as the GdO_{1.5} doping increases above 20 mol %, visible by the appearance of the F_g vibrational band, the *fluorite* volume fraction is diminished as the structure rearranges and clustering of vacancies to gadolinia doping cations prevails, “freezing” vacancies as “immobile” access points and reducing the oxygen ionic transport. We confirm here, now for thin film structures, an earlier trend, which coincides well with a report by Banerji *et al.*⁴² on the Raman spectra evolution of gadolinia-ceria powders. Furthermore, our results on the Ce_{1-x}Gd_xO_{2-y} thin films are in agreement with earlier structural investigations by Lubomirsky and co-workers on the solid solution system measured by EXAFS on powders, confirming that doping with gadolinia changes the local environment of Ce.⁴¹ Here, we show that the oxide thin films of the resistive switching devices present the structural features expected for devices with engineered oxygen vacancy configuration and mobility and turn now to the electrical characterization to measure their impact on the resistive switching.

Implication of Oxygen Vacancies on Resistive Switching Characteristics of the Ce_{1-x}Gd_xO_{2-y} Cross-Point Device Structures: Let’s Tailor the Vacancies Mobility and Configurational State. To clarify the role of the oxygen vacancy mobility and configuration for the oxygen ions to move in memristive devices in view of their resistive switching properties, we measure first exemplarily a Pt–Ce_{0.8}Gd_{0.2}O_{1.9- δ} –

Pt device in a microfabricated crossbar pattern by means of cyclic voltammetry. For this, we apply first an electroforming step in which a positive voltage is applied to the top electrode. This results in the formation of additional oxygen vacancies and electronic charge carriers (respectively Ce³⁺) near the bottom electrode, which decreases the resistance of the device and induces an asymmetry in defect concentrations, resulting in bipolar resistive switching (see [Supporting Information S3](#) for details). The cyclic voltammetry measurements reveal a pinched hysteretic current–voltage profile for voltages of ± 10 V (respectively, 20 MV/m) ([Figure 3a](#)). Applying a positive bias on the top electrode turns the device into a low-resistive “ON”-state, exhibiting counterclockwise also known as eightwise resistive switching. By reversing the bias polarity, the high-resistance “OFF”-state is reset. Depending on the applied bias history, two resistance states can be defined at the curve crossing with a resistance ratio of up to 100 for the Ce_{0.8}Gd_{0.2}O_{1.9- δ} switching units. Note that the slight shift of the curve crossing from the origin is caused by capacitive contributions similar to observations made for Pt–SrTiO₃–Pt memristive devices.⁵⁵ The stability is demonstrated over 50 cycles ([Figure 3b](#)), where the resistivity in the low-resistance ON- and high-resistance OFF-state is represented. The resistivity increases over the first 20 cycles, after which the values remain stable resulting in a $R_{\text{OFF}}/R_{\text{ON}}$ value of approximately 60 for more than 50 cycles. The resistance modulation is controlled by the device kinetics as the sweep rate dependence shows ([Figure 3c](#)). By increasing the cycling speed from 250 mV/s to 1 V/s, the resistance ratio decreases by approximately a factor of 5. Similar behavior was observed for Pt–SrTiO₃–Pt devices.⁵⁶ Importantly, the resistance \times area of our devices is independent of the electrode area for both the high and low resistive state ([Figure 3d](#)). The current–voltage curves are presented in the [Supporting Information](#), [Figure S3](#). This is also reflected in the $R_{\text{OFF}}/R_{\text{ON}}$ resistance ratio ([Figure 3e](#)). Comparison to results on Nb:STO⁴ confirms that the resistive switching process involves the whole electrode area

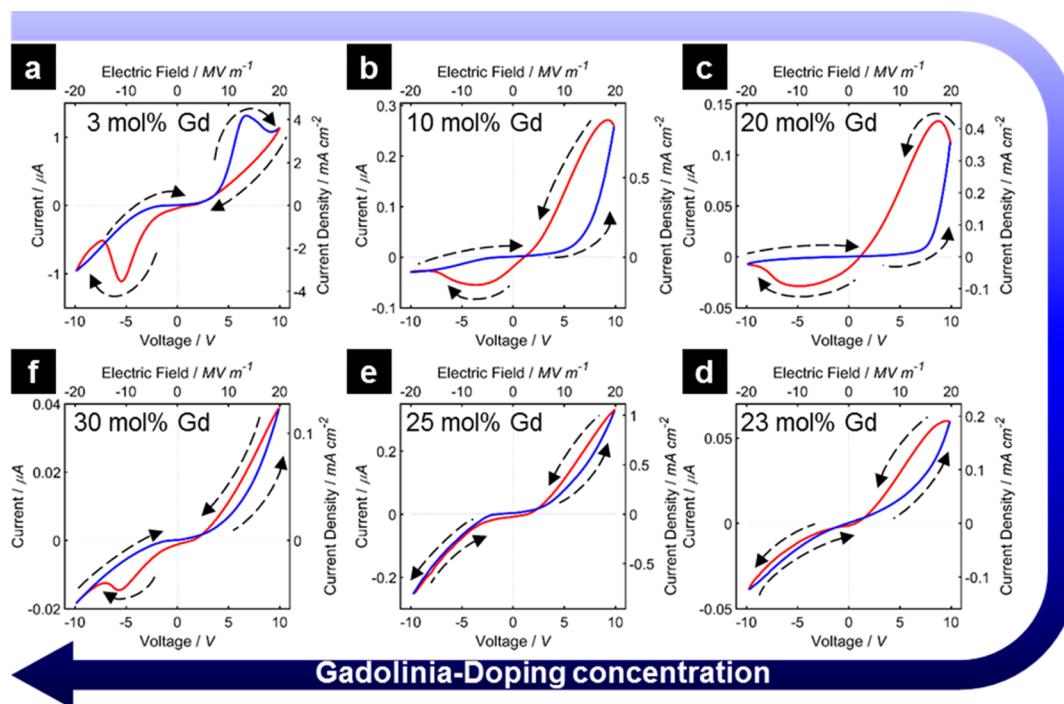


Figure 4. Current–voltage profiles of the gadolinia-doped ceria devices tailored in their oxygen vacancy concentration and configuration to alter the oxygen ionic conductivity in the oxide showing (a) no resistive switching for low doping concentrations and oxygen vacancies, (b,c) high resistive switching for intermediate doping concentrations with high oxygen ionic mobility, and (d–f) low resistive switching for high doping concentrations with reduced oxygen ionic mobility due to cluster formation.

and is not confined to a single conductive filament in gadolinia-doped ceria.

We demonstrate the successful operation of Pt–Ce_{0.8}Gd_{0.2}O_{1.9-δ}–Pt devices for resistive switching. In the following, we employ these test resistive switching structures to tailor the gadolinia extrinsic doping concentration in a systematic manner to study the implication of oxygen vacancy concentration and clustering on the resistive switching characteristics. Cyclic voltammetry measurements are performed, and the 25th out of 50 cycles is presented as an exemplary case for all doping concentrations as stable resistive switching is assured here (Figure 4). Here, we report the following observations by our successful defect engineering approach on the implication of the oxygen vacancy configuration and mobility on the resistive switching properties of the devices:

At low GdO_{1.5} doping concentration <10 mol % in ceria (Figure 4a), no crossing in the current–voltage profile is measured, and we ascribe the visible hysteresis to capacitive and volatile effects. In this state and according to Raman spectroscopy, a low level of oxygen vacancies is formed by adding the extrinsic doping. Due to the low level of oxygen vacancy concentration available for the oxygen ionic motion, an effective modulation of the electronic carrier concentration is minor. In essence, this demonstrates that there is a critical minimum oxygen vacancy concentration needed to induce resistive switching as if too low, simply capacitive effects and a nonlinear resistive behavior dominate in the current–voltage profile of the device.

At intermediate GdO_{1.5} doping concentration from 10 up to 20 mol % in ceria and enlarging the concentration of mobile oxygen vacancies (Figure 4b,c), a significant hysteresis in the current–voltage profile is measured showing the onset of oxygen ionic motion and as a result, resistive switching prevails

for the device. Remarkably, the strongest $R_{\text{OFF}}/R_{\text{ON}}$ ratio up to 100 was observed for an extrinsic doping concentration of 20 mol % GdO_{1.5} in ceria. This corresponds to the highest concentration of “free” oxygen vacancies and high oxygen ionic mobility in the pure fluorite structure.

Now, *high GdO_{1.5} doping concentrations up to 30 mol % in ceria (Figure 4d–f)* results in a reduced hysteretic opening and, thus, resistive switching of the device. In this extrinsic doping range, the $R_{\text{OFF}}/R_{\text{ON}}$ ratio is decreased reaching only a value of up to 2 for 30 mol % GdO_{1.5}. We interpret this finding by the reduced mobility of the oxygen ions to hop over vacancies that are “frozen” in clusters. In that case, we confirm that this coincides with the lowering of symmetry whereby the structure partially turns from fluorite to bixbyite measured by the appearance of the F_g Raman mode and pronounced shift in F_{2g} for the O–Ce–O stretching band (see Figure 2b for details).

We summarize the results in the box plot representation of the $R_{\text{OFF}}/R_{\text{ON}}$ resistance ratios for the different gadolinia concentrations of the ceria resistive switching devices (Figure 5). For every device, the results on five different electrodes are taken into account whenever resistive switching occurred. Only the measurements after the initial 20 stabilization cycles were considered. A maximum in the resistance $R_{\text{OFF}}/R_{\text{ON}}$ ratio is observed for *intermediate GdO_{1.5} doping concentrations* between 10 and 20 mol %. At *low* and *high* gadolinia doping concentrations, respectively, the $R_{\text{OFF}}/R_{\text{ON}}$ resistance ratio is very low with values around five. Comparing these results to the ionic conductivity at room temperature (data adapted from ref 39), we unequivocally demonstrate that there is a connection between the ionic conductivity of the oxide in resistive switching devices and the resistance $R_{\text{OFF}}/R_{\text{ON}}$ ratio. This analogy between ionic mobility and configuration of the vacancy type (“free” vs “clustered”) for the oxide and the

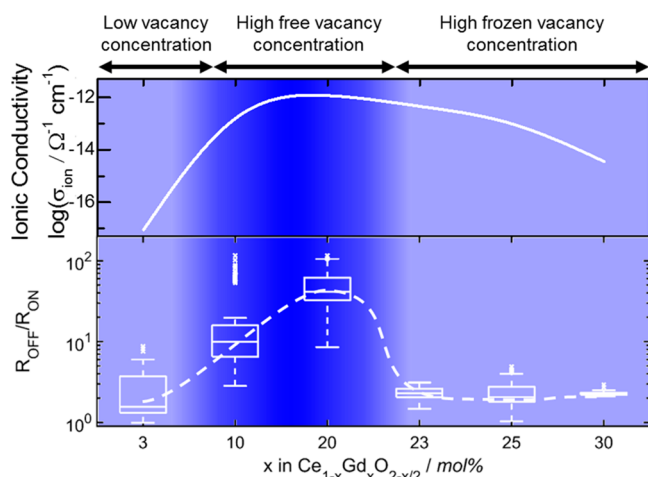


Figure 5. Box plot representation of the resistance ratio in gadolinia-doped ceria resistive switching device units for various gadolinia concentrations. A correlation between the $R_{\text{OFF}}/R_{\text{ON}}$ resistance ratio and the total ionic conductivity in the oxide is clearly visible. The total ionic conductivity data are extrapolated to room temperature, adapted from Tianshu *et al.*³⁹

resistive switching performance is shown in resistive switching devices.

In Figure 6, we schematically summarize the findings where the degree of oxygen vacancies is either “free” or “frozen” with

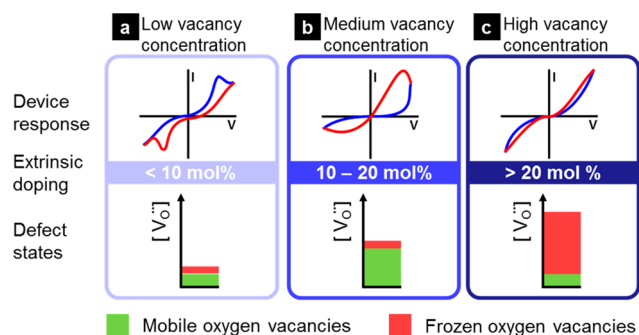


Figure 6. Schematic representation of the oxygen vacancy mobility regimes governing the memristive properties in gadolinia-doped ceria resistive switching devices. (a) At low doping concentrations, no switching is observed; the oxygen vacancy concentration is too low to modulate the device resistance. (b) At medium vacancy concentration, the high mobility of the oxygen vacancy defects enables the ionic motion that modulates the device resistance. (c) At high doping concentration, the ionic mobility is reduced through the formation of oxygen vacancies clusters, which results in a highly reduced resistive switching performance.

the device current–voltage response. At low $\text{GdO}_{1.5}$ doping concentration < 10 mol % (Figure 6a), where the concentration of oxygen vacancies is low, the number of mobile anionic carriers is insufficient to undergo reproducible resistive switching. The equivalent circuit model is governed by the capacitive contributions of the device. At intermediate $\text{GdO}_{1.5}$ doping concentration from 10 up to 20 mol % (Figure 6b), where the oxygen-ionic conductivity is at the maximum, we observe the largest memristive response with resistance ratios up to 100 for 20 mol % of $\text{GdO}_{1.5}$ doping. In that regime, the oxygen vacancies are present as “free” mobile defects, which govern resistive switching. At high $\text{GdO}_{1.5}$ doping concentrations up to 30

mol % (Figure 6c), the concentration of oxygen vacancies is high, but they are present as “frozen” defects, which reduces the oxygen ionic mobility as the association energy is too high. This, in turn, reduces the memristive response dramatically.

These results show a clear correlation between the concentration of mobile oxygen vacancies for the ions to hop and their degree of association not only for the ionic conductivity but for resistive switching. We highlight that the level of “free” versus “frozen” defects in the oxide is vital and needs to be carefully defect engineered for memristive devices.

Switching Model. We now propose a model to connect the findings to the defect chemistry of ceria. During the initial electroforming, oxygen ions probably migrate toward the top electrode where they accumulate and are released into the atmosphere. At the bottom electrode, oxygen vacancies accumulate, and their formal positive charge is balanced by Ce^{3+} , amplifying electronic conductivity in the resistive switching device. This reduction of gadolinia-doped ceria is possible as a result of the asymmetry of the device structure: the bottom electrode is engineered as buried under the oxide film, making it oxygen-blocking while the top Pt electrode is open and enables oxygen exchange with the atmosphere facilitated through the metal grain boundaries.⁵⁷

In the subsequent hysteretic current–voltage cycles, oxygen is redistributed within the structure under high electric fields. For positive bias, oxygen is transported to the top electrode, partially reducing the gadolinia-doped ceria, which leads to an increased electronic conductivity. When reversing the bias, the low resistive region of the material is reoxidized, and therefore, the electronic resistance is increased. This is possibly the physical origin of the polarity-dependent resistance modulation observed for intermediate doping concentrations in Figure 4b,c. Also, the significant dependence of the $R_{\text{OFF}}/R_{\text{ON}}$ ratio on the sweep rate shown in Figure 3c is in line with this model; at slower sweep rates, there is more time for ionic charge transfer, which increases the resistance ratio.

Hence, the modulation of the electronic current relies on mobile oxygen ions. By doping ceria with gadolinia, both the concentration and the mobility of the ionic carriers are modulated, as described earlier. Consequently, the doping concentration giving rise to the highest ionic conductivity is expected to show the largest resistance ratio, which is exactly what can be seen in Figure 5.

Here, we present a defect chemical model indicating the correlation between the ionic conductivity and the resistive switching performance on the example of the gadolinia-doped ceria solid solution. We demonstrate how the configuration of the oxygen vacancy defects in the memristive oxide steers the ionic motion underlying the resistance change in the devices.

CONCLUSION

In this study, we illustrate an effective correlation between the configurations of oxygen vacancy defects—set as either “free” or “clustered”—and the resistive switching performance for oxide-based resistive switching devices. The designed defect chemical methodology to tune not only the concentration but also the configuration of the defects by a tailored solid solution series for the oxide will be relevant to the engineering of memristors. The resistive switching performance has been shown to unequivocally scale with the oxygen ionic conductivity for the model devices based on gadolinia-doped ceria. The level of the extrinsic dopant, gadolinia, is either set to obtain a low concentration of oxygen vacancies showing almost

capacitive behavior in the current–voltage profile, a *high concentration of free and mobile oxygen vacancies* resulting in resistive switching, or, in the extreme case, *immobile associated oxygen vacancy defects* leading to a hampered ionic conductivity and resistive switching. In the latter case, symmetry breaks occur, and a transition from a *fluorite* to a *bixbyite* structure is measured due to the formation of immobile defect clusters of the oxygen vacancies in the oxide of the resistive switch. Importantly, extrinsic doping allows one to tune the concentration and mobility of oxygen vacancies in a much more systematic and controlled manner than what can be achieved through classic intrinsic defect variations such as oxygen-deficient deposition or postannealing for state-of-the-art resistive switching oxides. Careful engineering of switching oxides in their solid solution limits, association degree, and structural ordering of oxygen vacancy defects using extrinsic doping as a tool gives ample opportunities to engineer future high-performing memristors for memory and computing logics.

EXPERIMENTAL SECTION

The two-terminal memristive devices were fabricated by pulsed laser depositions of $\text{Ce}_{1-x}\text{Gd}_x\text{O}_{2-y}$ thin films sandwiched between two platinum electrodes in crossbar geometry.

Thin Film Preparation of the Resistive Switching Devices.

The $\text{Ce}_{1-x}\text{Gd}_x\text{O}_{2-y}$ ($x = 0.03\text{--}0.3$) thin films were deposited by pulsed laser deposition (PLD, Surface Advanced PLD technology; KrF excimer laser, 248 nm) operated at a target–substrate distance of 70 mm on round, randomly oriented sapphire substrates of 35 mm diameter (Stettler sapphire, Switzerland). The 500 nm thick films were deposited at 600 °C with a laser fluence of 0.54 J/cm² and 10 Hz repetition rate (20k shots) under constant oxygen flow at a pressure of 2.67×10^{-2} mbar.

The PLD targets of $\text{Ce}_{1-x}\text{Gd}_x\text{O}_{2-y}$ ($x = 0.03\text{--}0.3$) were prepared by solid-state synthesis, mixing stoichiometric amounts of CeO_2 (99.9%, Cerac specialty inorganics), $\text{Ce}_{0.9}\text{Gd}_{0.1}\text{O}_{1.95}$ (99.9%, Praxair), $\text{Ce}_{0.9}\text{Gd}_{0.2}\text{O}_{1.9}$ (99.9%, Praxair), and Gd_2O_3 (99.99%, Alfa Aesar). The powders were thoroughly mixed, pressed uniaxially at 4 MPa, and subsequently isostatically at 350 MPa for 2 min and sintered at 1400 °C for 24 h with heating and cooling rates of ± 5 °C/min. Phase purity was confirmed by XRD.

Resistive Switching Device Fabrication. The crossbar metal electrodes were patterned using a standard photolithography lift-off process in an ISO class 4 cleanroom. For this, the negative AZ nLOF 2020 (MicroChemicals, Germany) photoresist was spin-coated at a rotational speed of 4750 rpm for 45 s followed by a soft-bake at 110 °C for 60 s. The samples were then aligned (Karl-Süss MJB3 mask aligner) and exposed to broadband ultraviolet light (400 nm) with a dose of 320 mJ/cm² using a custom-made foil mask (Selba, Switzerland). After a postbaking at 110 °C for 60 s, the samples were developed for 90 s in AZ 726 (MIF) developer (MicroChemicals, Germany).

The metal electrodes were deposited by physical vapor deposition. First, the samples were cleaned in an O_2 plasma Asher (Technics Plasma TePla 100 Asher system) at 100 W and 1 mbar oxygen for 60 s. The bottom (5 nm Ti/80 nm Pt) and top (80 nm Pt) electrodes were then deposited by means of electron beam evaporation (Plassys MEB 550, France) with a substrate rotational speed of 4 rpm and a deposition rate of 1.5 Å/s. The lift-off process was done by soaking the samples subsequently in acetone and isopropyl alcohol.

Material Structural Characterization. The oxide's PLD target, as well as the thin film phase purity, was confirmed by X-ray diffraction (Bruker D8) at a $\text{Cu K}\alpha$ wavelength. The thin film microstructure was investigated by SEM (Zeiss LEO 1530, Germany) on device cross sections. A 4 nm Pt film was deposited on the cross sections to avoid charge buildup of the investigated surface. The surface morphology was measured by AFM (Cypher S, Asylum Research, USA) using AC tapping mode with an Arrow NCR tip (NanoWorld, Switzerland).

Ionic Near-Order Characterization. The anionic–cationic near-order structure was probed using a confocal WITec alpha300 R Raman microscope instrument (WITec, Germany) equipped with a 532 nm wavelength laser for excitation and a spectral resolution of 0.4 cm⁻¹. Fitting was done by OriginPro 9.0G using a Lorentzian function for the 465 cm⁻¹ peak and Gaussian for all others. An end points weighted background subtraction was chosen.

Electrical Characterization of Resistive Switch Device Elements. In this study, cyclic voltammetry was used to characterize the resistive switching performance of the model devices. The electrical measurements were carried out with a Keithley SMU 2601B in ambient conditions. In all measurements, the bias voltage was applied to the top electrode and the bottom electrode was grounded. The microelectrodes were contacted by platinum tips using micromanipulators.

Electroforming of Memristive Model Devices. A current-controlled electroforming was performed on all devices before the cyclic voltammetry measurements. The electroforming consists of applying 30 V with a compliance current of 30 mA/cm² (which corresponds to 100 μA for the standard electrodes of 100 μm radius). The duration of the electroforming was set to 300 s once the compliance current is reached, which was optimized to reach the highest conductivity after the electroforming, whereas the compliance current was chosen arbitrary and then applied to all the measurements for consistency.

Cyclic Voltammetry on Memristive Model Devices. Cyclic voltammetry measurements were carried out between ± 10 V (± 20 MV m⁻¹) with 500 mV s⁻¹ on circular electrodes with 100 μm in radii unless otherwise mentioned. The resistance of the resulting current–voltage curves is determined by fitting the data linearly at the intersection for both increasing and decreasing voltages.

ASSOCIATED CONTENT

Supporting Information

The Supporting Information is available free of charge on the ACS Publications website at DOI: 10.1021/acsnano.7b03116.

Defect chemistry of doped ceria; X-ray diffraction patterns of the thin film devices; Electroforming of pristine Pt– $\text{Ce}_{0.8}\text{Gd}_{0.2}\text{O}_{1.9-\delta}$ –Pt devices; Resistive switching of $\text{Ce}_{0.8}\text{Gd}_{0.2}\text{O}_{1.9-\delta}$ with varying electrode size (PDF)

AUTHOR INFORMATION

Corresponding Author

*E-mail: jrupp@mit.edu.

ORCID

Jennifer L.M. Rupp: 0000-0001-7160-0108

Notes

The authors declare no competing financial interest.

ACKNOWLEDGMENTS

The authors gratefully acknowledge Dr. A. Nennung for fruitful discussions. We thank Prof. P. Gambardella for the use of the atomic force microscope, Prof. A. Studart for the utilization of the secondary electron microscope, and Dr. M. Wörle for the use of the XRD facility. This work was supported by the Swiss National Science Foundation under the Project Numbers 155986 (SNSF (ERC) starting grant) and 138914. J.L.M.R. thanks the Thomas Lord Foundation for support of her Thomas Lord Assistant Professorship at the Department of Materials Science and Engineering (DMSE) at the Massachusetts Institute of Technology.

REFERENCES

- (1) Schwierz, F. Graphene Transistors. *Nat. Nanotechnol.* **2010**, *5*, 487–496.

- (2) Meijer, G. I. Who Wins the Nonvolatile Memory Race? *Science* **2008**, *319*, 1625–1626.
- (3) Traversa, F. L.; Di Ventra, M. Universal Memcomputing Machines. *IEEE Trans. Neural Netw. Learn. Syst.* **2015**, *26*, 2702.
- (4) Waser, R.; Dittmann, R.; Staikov, G.; Szot, K. Redox-Based Resistive Switching Memories – Nanoionic Mechanisms, Prospects, and Challenges. *Adv. Mater.* **2009**, *21*, 2632–2663.
- (5) Baeumer, C.; Schmitz, C.; Ramadan, A. H. H.; Du, H.; Skaja, K.; Feyer, V.; Muller, P.; Arndt, B.; Jia, C.-L.; Mayer, J.; De Souza, R. A.; Michael Schneider, C.; Waser, R.; Dittmann, R. Spectromicroscopic Insights for Rational Design of Redox-Based Memristive Devices. *Nat. Commun.* **2015**, *6*, 8610.
- (6) Kubicek, M.; Schmitt, R.; Messerschmitt, F.; Rupp, J. L. M. Uncovering Two Competing Switching Mechanisms for Epitaxial and Ultrathin Strontium Titanate-Based Resistive Switching Bits. *ACS Nano* **2015**, *9*, 10737–10748.
- (7) Acharyya, D.; Hazra, A.; Bhattacharyya, P. A Journey Towards Reliability Improvement of TiO₂ Based Resistive Random Access Memory: A Review. *Microelectron. Reliab.* **2014**, *54*, 541–560.
- (8) Goux, L.; Czarnecki, P.; Chen, Y. Y.; Pantisano, L.; Wang, X. P.; Degraeve, R.; Govoreanu, B.; Jurczak, M.; Wouters, D. J.; Altimime, L. Evidences of Oxygen-Mediated Resistive-Switching Mechanism in TiN/HfO₂/Pt Cells. *Appl. Phys. Lett.* **2010**, *97*, 243509.
- (9) Wei, Z.; Kanzawa, Y.; Arita, K.; Katoh, Y.; Kawai, K.; Muraoka, S.; Mitani, S.; Fujii, S.; Katayama, K.; Iijima, M.; Mikawa, T.; Ninomiya, T.; Miyanaga, R.; Kawashima, Y.; Tsuji, K.; Himeno, A.; Okada, T.; Azuma, R.; Shimakawa, K.; Sugaya, H.; et al. In Highly Reliable TaO_x ReRAM and Direct Evidence of Redox Reaction Mechanism, 2008 *IEEE International Electron Devices Meeting (IEDM)*; December 15–17, 2008; pp 1–4. DOI: 10.1109/IEDM.2008.4796676.
- (10) Yao, J.; Sun, Z.; Zhong, L.; Natelson, D.; Tour, J. M. Resistive Switches and Memories from Silicon Oxide. *Nano Lett.* **2010**, *10*, 4105–4110.
- (11) Kittl, J. A.; Opsomer, K.; Popovici, M.; Menou, N.; Kaczer, B.; Wang, X. P.; Adelman, C.; Pawlak, M. A.; Tomida, K.; Rothschild, A.; Govoreanu, B.; Degraeve, R.; Schaekers, M.; Zahid, M.; Delabie, A.; Meererschaut, J.; Polspoel, W.; Clima, S.; Pourtois, G.; Knaepen, W.; et al. High-k Dielectrics for Future Generation Memory Devices (Invited Paper). *Microelectron. Eng.* **2009**, *86*, 1789–1795.
- (12) Lee, S.; Lee, J. S.; Park, J.-B.; Koo Kyoung, Y.; Lee, M.-J.; Won Noh, T. Anomalous Effect Due to Oxygen Vacancy Accumulation Below the Electrode in Bipolar Resistance Switching Pt/Nb:SrTiO₃ Cells. *APL Mater.* **2014**, *2*, 066103.
- (13) Park, J.; Kwon, D.-H.; Park, H.; Jung, C. U.; Kim, M. Role of Oxygen Vacancies in Resistive Switching in Pt/Nb-Doped SrTiO₃. *Appl. Phys. Lett.* **2014**, *105*, 183103.
- (14) Menzel, S.; Waters, M.; Marchewka, A.; Böttger, U.; Dittmann, R.; Waser, R. Origin of the Ultra-Nonlinear Switching Kinetics in Oxide-Based Resistive Switches. *Adv. Funct. Mater.* **2011**, *21*, 4487–4492.
- (15) Bae, Y. C.; Lee, A. R.; Kwak, J. S.; Im, H.; Hong, J. P. Dependence of Resistive Switching Behaviors on Oxygen Content of the Pt/TiO_{2-x}/Pt Matrix. *Curr. Appl. Phys.* **2011**, *11*, e66–e69.
- (16) Sharath, S. U.; Bertaud, T.; Kurian, J.; Hildebrandt, E.; Walczyk, C.; Calka, P.; Zaumseil, P.; Sowinska, M.; Walczyk, D.; Gloskovskii, A.; Schroeder, T.; Alff, L. Towards Forming-Free Resistive Switching in Oxygen Engineered HfO_{2-x}. *Appl. Phys. Lett.* **2014**, *104*, 063502.
- (17) Younis, A.; Chu, D.; Li, S. Oxygen Level: the Dominant of Resistive Switching Characteristics in Cerium Oxide Thin Films. *J. Phys. D: Appl. Phys.* **2012**, *45*, 355101.
- (18) Kwak, J. S.; Do, Y. H.; Bae, Y. C.; Im, H.; Hong, J. P. Reproducible Unipolar Resistive Switching Behaviors in the Metal-Deficient CoO_x Thin Film. *Thin Solid Films* **2010**, *518*, 6437–6440.
- (19) Li, J.-C.; Hou, X.-Y.; Cao, Q. Effect of Cu Doping on the Resistive Switching of NiO Thin Films. *J. Appl. Phys.* **2014**, *115*, 164507.
- (20) Zhang, H.; Liu, L.; Gao, B.; Qiu, Y.; Liu, X.; Lu, J.; Han, R.; Kang, J.; Yu, B. Gd-Doping Effect on Performance of HfO₂ Based Resistive Switching Memory Devices Using Implantation Approach. *Appl. Phys. Lett.* **2011**, *98*, 042105.
- (21) Kim, S.; Choi, S.; Lee, J.; Lu, W. D. Tuning Resistive Switching Characteristics of Tantalum Oxide Memristors through Si Doping. *ACS Nano* **2014**, *8*, 10262–10269.
- (22) Wang, Z.-H.; Yang, Y.; Gu, L.; Habermeier, H. U.; Yu, R.-C.; Zhao, T.-Y.; Sun, J.-R.; Shen, B.-G. Correlation Between Evolution of Resistive Switching and Oxygen Vacancy Configuration in La_{0.5}Ca_{0.5}MnO₃ Based Memristive Devices. *Nanotechnology* **2012**, *23*, 265202.
- (23) Kim, Y. S.; Kim, J.; Yoon, M. J.; Sohn, C. H.; Buhm Lee, S.; Lee, D.; Chul Jeon, B.; Keun Yoo, H.; Won Noh, T.; Bostwick, A.; Rotenberg, E.; Yu, J.; Don Bu, S.; Simon Mun, B. Impact of Vacancy Clusters on Characteristic Resistance Change of Nonstoichiometric Strontium Titanate Nano-Film. *Appl. Phys. Lett.* **2014**, *104*, 013501.
- (24) Mogensen, M.; Sammes, N. M.; Tompsett, G. A. Physical, Chemical and Electrochemical Properties of Pure and Doped Ceria. *Solid State Ionics* **2000**, *129*, 63–94.
- (25) Ruiz-Trejo, E.; Maier, J. Electronic Transport in Single Crystals of Gd-Doped Ceria. *J. Electrochem. Soc.* **2007**, *154*, B583–B587.
- (26) Feng, Z. A.; El Gabaly, F.; Ye, X.; Shen, Z. X.; Chueh, W. C. Fast Vacancy-Mediated Oxygen Ion Incorporation Across the Ceria-Gas Electrochemical Interface. *Nat. Commun.* **2014**, *5*, 4374.
- (27) Kuhn, M.; Bishop, S. R.; Rupp, J. L. M.; Tuller, H. L. Structural Characterization and Oxygen Nonstoichiometry of Ceria-Zirconia (Ce_{1-x}Zr_xO_{2-δ}) Solid Solutions. *Acta Mater.* **2013**, *61*, 4277–4288.
- (28) Yang, N.; Shi, Y.; Schweiger, S.; Strelcov, E.; Belianinov, A.; Foglietti, V.; Orgiani, P.; Balestrino, G.; Kalinin, S. V.; Rupp, J. L. M.; Aruta, C. Role of Associated Defects in Oxygen Ion Conduction and Surface Exchange Reaction for Epitaxial Samaria-Doped Ceria Thin Films as Catalytic Coatings. *ACS Appl. Mater. Interfaces* **2016**, *8*, 14613–14621.
- (29) Shi, Y.; Bork, A. H.; Schweiger, S.; Rupp, J. L. M. The Effect of Mechanical Twisting on Oxygen Ionic Transport in Solid-State Energy Conversion Membranes. *Nat. Mater.* **2015**, *14*, 721–727.
- (30) Rupp, J. L. M.; Gauckler, L. J. Microstructures and Electrical Conductivity of Nanocrystalline Ceria-Based Thin Films. *Solid State Ionics* **2006**, *177*, 2513–2518.
- (31) Jasinski, P.; Suzuki, T.; Anderson, H. U. Nanocrystalline Undoped Ceria Oxygen Sensor. *Sens. Actuators, B* **2003**, *95*, 73–77.
- (32) Almar, L.; Tarancón, A.; Andreu, T.; Torrell, M.; Hu, Y.; Dezanneau, G.; Morata, A. Mesoporous Ceramic Oxides as Humidity Sensors: A Case Study for Gadolinium-Doped Ceria. *Sens. Actuators, B* **2015**, *216*, 41–48.
- (33) Ackermann, S.; Sauvin, L.; Castiglioni, R.; Rupp, J. L. M.; Scheffe, J. R.; Steinfeld, A. Kinetics of CO₂ Reduction over Nonstoichiometric Ceria. *J. Phys. Chem. C* **2015**, *119*, 16452–16461.
- (34) Chueh, W. C.; Falter, C.; Abbott, M.; Scipio, D.; Furler, P.; Haile, S. M.; Steinfeld, A. High-Flux Solar-Driven Thermochemical Dissociation of CO₂ and H₂O Using Nonstoichiometric Ceria. *Science* **2010**, *330*, 1797–1801.
- (35) Rupp, J. L. M.; Fabbri, E.; Marrocchelli, D.; Han, J.-W.; Chen, D.; Traversa, E.; Tuller, H. L.; Yildiz, B. Scalable Oxygen-Ion Transport Kinetics in Metal-Oxide Films: Impact of Thermally Induced Lattice Compaction in Acceptor Doped Ceria Films. *Adv. Funct. Mater.* **2014**, *24*, 1562–1574.
- (36) Ruiz-Trejo, E. The Optical Band Gap of Gd-Doped CeO₂ Thin Films as Function of Temperature and Composition. *J. Phys. Chem. Solids* **2013**, *74*, 605–610.
- (37) Ou, D. R.; Mori, T.; Ye, F.; Zou, J.; Auchterlonie, G.; Drennan, J. Oxygen-Vacancy Ordering in Lanthanide-Doped Ceria: Dopant-Type Dependence and Structure Model. *Phys. Rev. B: Condens. Matter Phys.* **2008**, *77*, 024108.
- (38) Li, Z.-P.; Mori, T.; Ye, F.; Ou, D. R.; Zou, J.; Drennan, J. Structural Phase Transformation Through Defect Cluster Growth in Gd-Doped Ceria. *Phys. Rev. B: Condens. Matter Phys.* **2011**, *84*, 180201.

- (39) Tianshu, Z.; Hing, P.; Huang, H.; Kilner, J. Ionic Conductivity in the CeO₂-Gd₂O₃ System (0.05 ≤ Gd/Ce ≤ 0.4) Prepared by Oxalate Coprecipitation. *Solid State Ionics* **2002**, *148*, 567–573.
- (40) Artini, C.; Pani, M.; Carnasciali, M. M.; Buscaglia, M. T.; Plaisier, J. R.; Costa, G. A. Structural Features of Sm- and Gd-Doped Ceria Studied by Synchrotron X-ray Diffraction and μ -Raman Spectroscopy. *Inorg. Chem.* **2015**, *54*, 4126–4137.
- (41) Kossov, A.; Wang, Q.; Korobko, R.; Grover, V.; Feldman, Y.; Wachtel, E.; Tyagi, A. K.; Frenkel, A. I.; Lubomirsky, I. Evolution of the Local Structure at the Phase Transition in CeO₂-Gd₂O₃ Solid Solutions. *Phys. Rev. B: Condens. Matter Mater. Phys.* **2013**, *87*, 054101.
- (42) Banerji, A.; Grover, V.; Sathe, V.; Deb, S. K.; Tyagi, A. K. CeO₂-Gd₂O₃ System: Unraveling of Microscopic Features by Raman Spectroscopy. *Solid State Commun.* **2009**, *149*, 1689–1692.
- (43) Schweiger, S.; Kubicek, M.; Messerschmitt, F.; Murer, C.; Rupp, J. L. M. A Microdot Multilayer Oxide Device: Let Us Tune the Strain-Ionic Transport Interaction. *ACS Nano* **2014**, *8*, 5032–5048.
- (44) Schweiger, S.; Pfenninger, R.; Bowman, W. J.; Aschauer, U.; Rupp, J. L. M. Designing Strained Interface Heterostructures for Memristive Devices. *Adv. Mater.* **2017**, *29*, 1605049.
- (45) Lin, C.-Y.; Lee, D.-Y.; Wang, S.-Y.; Lin, C.-C.; Tseng, T.-Y. Reproducible Resistive Switching Behavior in Sputtered CeO₂ Polycrystalline Films. *Surf. Coat. Technol.* **2008**, *203*, 480–483.
- (46) Seong, D.-j.; Jo, M.; Lee, D.; Hwang, H. HPHA Effect on Reversible Resistive Switching of Pt/Nb -Doped SrTiO₃ Schottky Junction for Nonvolatile Memory Application. *Electrochem. Solid-State Lett.* **2007**, *10*, H168–H170.
- (47) Gao, P.; Wang, Z.; Fu, W.; Liao, Z.; Liu, K.; Wang, W.; Bai, X.; Wang, E. *In situ* TEM Studies of Oxygen Vacancy Migration for Electrically Induced Resistance Change Effect in Cerium Oxides. *Micron* **2010**, *41*, 301–305.
- (48) Ortega-Hernandez, R.; Coll, M.; Gonzalez-Rosillo, J.; Palau, A.; Obradors, X.; Miranda, E.; Puig, T.; Suñe, J. Resistive Switching in CeO₂/La_{0.8}Sr_{0.2}MnO₃ Bilayer for Non-Volatile Memory Applications. *Microelectron. Eng.* **2015**, *147*, 37–40.
- (49) McBride, J. R.; Hass, K. C.; Poindexter, B. D.; Weber, W. H. Raman and X-ray Studies of Ce_{1-x}RE_xO_{2-y}, where RE = La, Pr, Nd, Eu, Gd, and Tb. *J. Appl. Phys.* **1994**, *76*, 2435–2441.
- (50) Artini, C.; Costa, G. A.; Pani, M.; Lausi, A.; Plaisier, J. Structural Characterization of the CeO₂/Gd₂O₃ Mixed System by Synchrotron X-ray Diffraction. *J. Solid State Chem.* **2012**, *190*, 24–28.
- (51) White, W. B.; Keramidis, V. G. Vibrational Spectra of Oxides with the C-Type Rare Earth Oxide Structure. *Spectrochim. Acta, Part A* **1972**, *28*, 501–509.
- (52) Urban, M. W.; Cornilsen, B. C. Bonding Anomalies in the Rare Earth Sesquioxides. *J. Phys. Chem. Solids* **1987**, *48*, 475–479.
- (53) Nakajima, A.; Yoshihara, A.; Ishigame, M. Defect-Induced Raman Spectra in Doped CeO₂. *Phys. Rev. B: Condens. Matter Mater. Phys.* **1994**, *50*, 13297–13307.
- (54) Dilawar, N.; Varandani, D.; Mehrotra, S.; Poswal, H. K.; Sharma, S. M.; Bandyopadhyay, A. K. Anomalous High Pressure Behaviour in Nanosized Rare Earth Sesquioxides. *Nanotechnology* **2008**, *19*, 115703.
- (55) Messerschmitt, F.; Kubicek, M.; Rupp, J. L. M. How Does Moisture Affect the Physical Property of Memristance for Anionic-Electronic Resistive Switching Memories? *Adv. Funct. Mater.* **2015**, *25*, 5117–5125.
- (56) Messerschmitt, F.; Kubicek, M.; Schweiger, S.; Rupp, J. L. M. Memristor Kinetics and Diffusion Characteristics for Mixed Anionic-Electronic SrTiO_{3,δ} Bits: The Memristor-Based Cottrell Analysis Connecting Material to Device Performance. *Adv. Funct. Mater.* **2014**, *24*, 7448–7460.
- (57) Opitz, A. K.; Lutz, A.; Kubicek, M.; Kubel, F.; Hutter, H.; Fleig, J. Investigation of the Oxygen Exchange Mechanism on Ptltytria Stabilized Zirconia at Intermediate Temperatures: Surface Path versus Bulk Path. *Electrochim. Acta* **2011**, *56*, 9727–9740.
- (58) Dou, C.; Kakushima, K.; Ahmet, P.; Tsutsui, K.; Nishiyama, A.; Sugii, N.; Natori, K.; Hattori, T.; Iwai, H. Resistive Switching Behavior of a CeO₂ Based ReRAM Cell Incorporated with Si Buffer Layer. *Microelectron. Reliab.* **2012**, *52*, 688–691.
- (59) Chundak, M.; Yoshitake, M.; Vaclavu, M.; Matolin, V.; Chikyow, T. Influence of Chemical Equilibrium in Introduced Oxygen Vacancies on Resistive Switching in Epitaxial Pt-CeO₂ System. *J. Solid State Electrochem.* **2017**, *21*, 657.
- (60) Liu, L. F.; Sun, X.; Sun, B.; Kang, J. F.; Wang, Y.; Liu, X. Y.; Han, R. Q.; Xiong, G. C. In Current Compliance-Free Resistive Switching in Nonstoichiometric CeO_x Films for Nonvolatile Memory Application; *2009 IEEE International Memory Workshop (IMW)*, May 10–14, 2009; pp 1–2. DOI: 10.1109/IMW.2009.5090586.
- (61) Liao, Z.-L.; Chen, D.-M. A Metal Oxide Heterostructure for Resistive Random Access Memory Devices. *Chin. Phys. Lett.* **2013**, *30*, 047701.
- (62) Velichko, A.; Boriskov, P.; Savenko, A.; Grishin, A.; Khartsev, S.; Yar, M. A.; Muhammed, M. Memory Resistive Switching in CeO₂-Based Film Microstructures Patterned by a Focused Ion Beam. *Thin Solid Films* **2014**, *556*, 520–524.
- (63) Fors, R.; Khartsev, S. I.; Grishin, A. M. Giant Resistance Switching in Metal-Insulator-Manganite Junctions: Evidence for Mott Transition. *Phys. Rev. B: Condens. Matter Mater. Phys.* **2005**, *71*, 045305.
- (64) Zhang, J.; Zhao, H.; Wei, F.; Yang, M.; Yang, Z.; Chen, Q.; Chen, J. Resistive Switching Behaviour of Highly Epitaxial CeO₂ Thin Film for Memory Application. *Phys. Status Solidi RRL* **2014**, *8*, 95–99.
- (65) Ismail, M.; Talib, I.; Rana, A. M.; Ahmed, E.; Nadeem, M. Y. Performance Stability and Functional Reliability in Bipolar Resistive Switching of Bilayer Ceria Based Resistive Random Access Memory Devices. *J. Appl. Phys.* **2015**, *117*, 084502.
- (66) Zhou, Q.; Zhai, J. Study of the Resistive Switching Characteristics and Mechanisms of Pt/CeO_x/TiN Structure for RRAM Applications. *Integr. Ferroelectr.* **2012**, *140*, 16–22.
- (67) Pan, T. M.; Lu, C. H. Switching Behavior in Rare-Earth Films Fabricated in Full Room Temperature. *IEEE Trans. Electron Devices* **2012**, *59*, 956–961.
- (68) Younis, A.; Chu, D.; Li, S. Stochastic Memristive Nature in Co-Doped CeO₂ Nanorod Arrays. *Appl. Phys. Lett.* **2013**, *103*, 253504.
- (69) Chen, X. G.; Fu, J. B.; Li, L. Z.; Yun, C.; Zhao, H.; Zhang, X. F.; Wang, C. S.; Yang, Y. C.; Yang, J. B. Resistive Switching Effects in CeO₂/La_{0.7}(Sr_{0.1}Ca_{0.9})_{0.3}MnO₃/Pt Heterostructures Prepared by Pulse Laser Deposition Method. *Phys. Lett. A* **2014**, *378*, 2561–2564.
- (70) Zhu, Y.; Li, M.; Zhou, H.; Hu, Z.; Liu, X.; Liao, H. Improved Bipolar Resistive Switching Properties in CeO₂/ZnO Stacked Heterostructures. *Semicond. Sci. Technol.* **2013**, *28*, 015023.